

## Nonequilibrium phase transition in a driven-dissipative quantum antiferromagnet

Mona H. Kalthoff,<sup>1,\*</sup> Dante M. Kennes,<sup>2,3,1,†</sup> Andrew J. Millis,<sup>4,5,‡</sup> and Michael A. Sentef<sup>1,§</sup><sup>1</sup>Max Planck Institute for the Structure and Dynamics of Matter, Center for Free Electron Laser Science, Luruper Chaussee 149, 22761 Hamburg, Germany<sup>2</sup>Institut für Theorie der Statistischen Physik, RWTH Aachen University, 52056 Aachen, Germany<sup>3</sup>JARA-Fundamentals of Future Information Technology, 52056 Aachen, Germany<sup>4</sup>Department of Physics, Columbia University, 538 West 120th Street, New York, New York 10027, USA<sup>5</sup>Center for Computational Quantum Physics, Flatiron Institute, 162 5th Avenue, New York, New York 10010, USA

(Received 15 December 2021; accepted 19 April 2022; published 12 May 2022)

A deeper theoretical understanding of driven-dissipative interacting systems and their nonequilibrium phase transitions is essential both to advance our fundamental physics understanding and to harness technological opportunities arising from optically controlled quantum many-body states. This paper provides a numerical study of dynamical phases and the transitions between them in the nonequilibrium steady state of the prototypical two-dimensional Heisenberg antiferromagnet with drive and dissipation. We demonstrate a nonthermal transition that is characterized by a qualitative change in the magnon distribution from subthermal at low drive to a generalized Bose-Einstein form including a nonvanishing condensate fraction at high drive. A finite-size analysis reveals static and dynamical critical scaling at the transition, with a discontinuous slope of the magnon number versus driving field strength and critical slowing down at the transition point. Implications for experiments on quantum materials and polariton condensates are discussed.

DOI: [10.1103/PhysRevResearch.4.023115](https://doi.org/10.1103/PhysRevResearch.4.023115)

## I. INTRODUCTION

Nonequilibrium phase transitions in driven interacting quantum systems constitute a fundamental and largely open research problem [1,2]. *Quenches*, i.e., abrupt changes in Hamiltonian parameters or initial conditions, followed by a time evolution, have been extensively studied and can lead to dynamical phase transitions [3,4] characterized by qualitative modifications of the dynamical response as the quench magnitude is varied. A nonequilibrium steady state presents additional issues involving the flow and redistribution of energy: the drive adds energy, the dissipation removes energy, and the internal dynamics redistribute energy among modes [5,6]. As the drive strength is varied, the competition between these effects can qualitatively change system properties in the same sense that changing temperature or a Hamiltonian parameter can drive a system through an equilibrium phase transition.

Equilibrium phase transitions are typically analyzed in terms of the onset or disappearance of order parameters that encode broken symmetries, for example, the staggered

magnetization in an antiferromagnet that appears when the temperature is reduced below a critical temperature. We label such phase transitions as symmetry-breaking transition in the following. In a nonequilibrium setting, an additional type of phase transition can exist that is characterized by a qualitative change in the low-frequency distribution of the collective excitations of a system. Such a transition cannot exist in equilibrium where the form of the distribution is fixed by equilibrium thermodynamics. We refer to the latter as a subthermal-to-superthermal transition. Phase transitions occurring in a nonequilibrium *steady state* are the subject of an interesting and growing body of literature [7–15] but are less well understood. A deeper theoretical understanding of these issues could open nonthermal pathways for controlling emergent properties of driven quantum materials [2].

Driven magnetic systems are of particular interest in this context for both fundamental and technological reasons [16]. A specific focus of attention has been the possibility of magnon Bose-Einstein condensation (BEC), in which a system is excited by a radiation pulse and the resulting excitation distribution forms a single coherent macroscopic quantum state with the lowest-energy excited state being macroscopically populated. The existing experimental literature on magnon BEC [17–32] concerns systems with very long energy relaxation times, in which a population of magnons is transiently induced (often by a short-duration frequency-coherent excitation) and then evolves into a BEC [16,33–35]. This physics is very similar to the Bose-Einstein condensation of excitons and exciton-polaritons which has been studied experimentally [36–40] and theoretically [41–43]. Theoretical analyses of the magnon case to date have been based on semiphenomenological continuum approximations using

\*mona.kalthoff@mpsd.mpg.de

†dante.kennes@rwth-aachen.de

‡amillis@flatironinstitute.org

§michael.sentef@mpsd.mpg.de

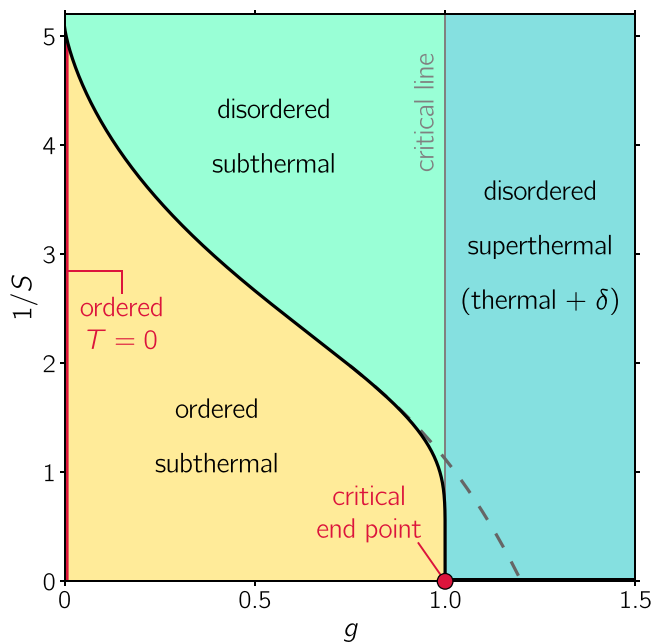


FIG. 1. Nonequilibrium phase diagram of driven-dissipative steady states. Steady states as a function of drive strength  $g$  and quantum fluctuations, parametrized here by the inverse spin length  $1/S$  but controlled in physical systems by many factors, including geometrical frustration. The red section along the vertical axis marks the antiferromagnetically ordered ground state at  $T = 0$ . The black curve separating the ordered (orange) and disordered (green) subthermal phases is obtained by determining the value of  $1/S$  at which the staggered magnetization [as defined in Eq. (A10)] vanishes for a given  $g$ . The gray vertical line at  $g = 1$  separates the subthermal regime from the superthermal regime, which turns into a thermal distribution plus a  $\delta$ -function in the interacting system in the thermodynamic limit. The critical end point at  $g = 1$ ,  $1/S = 0$  is a specific feature of the Heisenberg antiferromagnet in two dimensions. The gray dashed curve indicates the expected behavior in three dimensions or in the anisotropic  $xy$  or  $xxz$  (Ising, gapped) regimes in two dimensions.

Landau-Lifshitz-Gilbert equations [44,45], Gross-Pitaevskii equations [18,26,27], or field theoretical analyses [8,10,12–15,42,43]. Here, we focus on the distribution function of excitations.

In this work we aim to add a new dimension to the understanding of this field. We study a steady-state system in which the crucial physics is the interplay of interactions and the flow of energy and particles from the drive through the system to a dissipative reservoir. We provide a precise microscopic treatment of the interaction among excitations, which is known [35,46–57] to be crucial for the long-time physics. Figure 1 shows the behavior of the spin system under consideration as a function of the critical parameter  $g$ , which parametrizes the nonequilibrium excitation strength relative to dissipative losses and will be introduced in more detail below. Figure 1 displays two distinct phase transitions, namely, an order-to-disorder phase transition, which is conceptually similar to known equilibrium transitions but occurs here for nonthermal distributions, and an intrinsically nonequilibrium subthermal-to-superthermal transition, which we study in this paper. The

latter phase transition is characterized by a qualitative change in the distribution function.

## II. MODEL AND FORMALISM

### A. Hamiltonian and kinetic equation

We study the driven-dissipative square-lattice Heisenberg antiferromagnet with nearest-neighbor interactions, described by the Hamiltonian

$$H_{\text{Heis}} = J \sum_{\langle ij \rangle} \left\{ \frac{1}{2} (S_i^+ S_j^- + S_i^- S_j^+) + S_i^z S_j^z \right\}, \quad (1)$$

with canonical spin operators  $S_i$  at site  $i$  of the lattice. The Heisenberg Hamiltonian has two parameters, the exchange coupling strength  $J$ , which sets the energy scale and which we take to be positive so that the ground state is antiferromagnetic, and the spin magnitude  $|S|$ , which sets the strength of the quantum fluctuations and of the interactions between the spin waves. At  $|S| = \infty$  the model is straightforwardly solvable and has a twofold degenerate set of spin-wave excitations (magnons) with dispersion  $\omega_k$ . The primary object of interest will be the magnon distribution function  $n_k$  counting the number of magnons excited above the ground state into the mode with energy  $\omega_k$ . Key to our analysis will be the interactions between magnons. Because we are interested in the qualitative effects of the interactions, we use a standard Holstein-Primakoff method [58] to obtain the spin-wave interactions at leading nontrivial order in  $1/|S|$  (see Appendix A). The important points here are that the inter-spin-wave interactions conserve both total energy and the total number of spin waves and that their effect on the distribution may be studied using the Boltzmann equation with a collision integral  $\mathcal{S}$  derived via standard methods from the magnon-magnon interactions.

The Heisenberg model is an effective model describing the low-energy physics of a more fundamental system of strongly correlated electrons moving in a periodic lattice potential such as the Hubbard model. These more fundamental models enable a calculation of the drive due to electromagnetic radiation and dissipation due to coupling with a reservoir. We specifically adopt the model studied in Ref. [59] in which the Heisenberg model is obtained as the low-energy limit of the half-filled large- $U$  Hubbard model. The drive emerges from a Floquet analysis of minimally coupled high-frequency radiation detuned from the upper Hubbard band. The dissipation results from particle exchange with a reservoir, which we take to be at zero temperature. The particle exchange is virtual because of the Mott-Hubbard gap, but dissipation of energy and magnons into the reservoir is allowed.

Since we consider only a spatially uniform drive, we restrict our attention to a distribution function of energy  $\omega$  (instead of momentum  $\mathbf{k}$ ) defined [60] as  $n(\omega) = \int d^2k n_k \delta(\omega - \omega_k) / \rho(\omega)$ , with  $\omega_k$  being the magnon energy and  $n_k$  being the magnon distribution as a function of wave vector. The density of states summed over the two magnon branches is

$$\rho(\omega) = 2 \int d^2k \delta(\omega - \omega_k). \quad (2)$$

We take the drive and dissipation from a previous analysis [59] of the driven-dissipative Hubbard model, specializing it

to the particular case of a high-frequency drive detuned from any charge excitations and a dissipation arising from particle exchange with a reservoir. Reference [59] found, using an approximation that neglected the magnon-magnon interactions, that the effect of a high-frequency detuned drive is the addition of magnons to the system, such that the number of magnons in the mode with energy  $\omega$  increases at the rate  $\gamma_{\text{in}}[1 + n(\omega)]$ .  $\gamma_{\text{in}}$  is proportional to the drive strength, and the simple form of the in-scattering follows from the very high frequency, detuned drive. The calculation also implies a decay of magnons into the charge reservoir at a rate given by  $\gamma_{\text{out}}[n(\omega) + (\frac{n(\omega)}{n_{\tilde{T}}(\omega)})^2]$ , with  $n_{\tilde{T}}(\omega) = 1/(e^{\frac{\omega}{\tilde{T}}} - 1)$  and parameter  $\tilde{T} \approx 0.6J$ . Note that  $\tilde{T}$  from Eq. (3) is not the equilibrium temperature of the system but is a parameter describing the nonlinearity of the relaxation to the bath. The nonlinearity ensures a steady state at any drive amplitude. The key features of the out-scattering are that the basic rate is determined by the particle-reservoir coupling and that the nonlinearity vanishes quadratically as  $\omega_k \rightarrow 0$ . The latter feature stems from the large charge gap and the vanishing of the charge-magnon coupling at low energies due to the Goldstone theorem.

This allows us to write down a kinetic equation that encodes magnon-magnon scattering through the collision integral  $\mathcal{S}$  as well as the effects of drive and dissipation,

$$\partial_t n(\omega) = \gamma_{\text{in}}[1 + n(\omega)] - \gamma_{\text{out}} \left[ n(\omega) + \left( \frac{n(\omega)}{n_{\tilde{T}}(\omega)} \right)^2 \right] + \mathcal{S}\{n(\omega)\}. \quad (3)$$

### B. Numerical implementation

We discretize the system and solve the resulting set of coupled nonlinear equations numerically by integrating forward in time from an initial condition until a steady state is reached. We choose a uniform  $\ell \times \ell$  momentum space grid containing  $N = \ell^2$  points, as shown in Appendix D, and therefore a discrete set of momentum points  $\omega_k$ . We replace all momentum/frequency integrals by sums. The largest linear dimension  $\ell$  used throughout the paper is  $\ell = 120$ , which is the default discretization parameter for the results shown below, unless otherwise indicated. The discretized momentum grid is chosen in a way such that  $\mathbf{k} = 0$  is avoided because a Bose-Einstein distribution with  $\mu = 0$  diverges as  $\mathbf{k} \rightarrow 0$ , implying that  $\mathbf{k} = 0$  cannot be treated directly numerically (see Appendix D, Fig. 7). Below we employ a careful finite-size scaling analysis and extrapolation to infinite system size to extract information about  $\mathbf{k} \rightarrow 0$  and possible Bose-Einstein condensation. In the numerical results presented here we fix the parameter  $\tilde{T}$  describing the nonlinear term in the dissipation as  $\tilde{T} = 0.6$  and set  $\gamma_{\text{out}} = 0.002$ , unless explicitly denoted otherwise. Our conclusions are independent of the specific parameter values.

As noted above, the collision integral  $\mathcal{S}$  conserves the magnon number  $\mathcal{N}$  and energy  $\mathcal{E}$ , which are discretized as

$$\mathcal{N} = \sum_{m=1}^{\omega_{\text{max}}} \rho(\omega_m) n(\omega_m), \quad (4a)$$

$$\mathcal{E} = \sum_{m=1}^{\omega_{\text{max}}} \rho(\omega_m) n(\omega_m) \omega_m, \quad (4b)$$

where  $\rho(\omega_m)$  is the discretization of the density of states given in Eq. (2). We parametrize the drive strength via the dimensionless tuning parameter, which controls the excitation density,

$$g \equiv \frac{\gamma_{\text{in}}}{\gamma_{\text{out}}}, \quad (5)$$

and consider the qualitative form of the computed magnon distribution function.

## III. RESULTS

### A. Nonequilibrium phase diagram

Figure 1 summarizes our findings in terms of a phase diagram in the plane defined by the amplitude of quantum fluctuations (inverse spin length  $1/S$ , vertical axis) and the drive strength  $g$  (horizontal axis). In equilibrium ( $g = 0$ ), increasing quantum fluctuations drives a transition to a quantum disordered state. Increasing the drive strength at a fixed value of quantum fluctuations produces two conceptually distinct effects.

The drive adds energy to the system, exciting magnons above the ground state and thereby weakening the order. For drive strengths less than a critical value (here,  $g = 1$ ) the magnon distribution retains a subthermal form, with the magnon occupation  $n(\omega)$  remaining finite as the magnon energy  $\omega$  vanishes, in contrast to the  $\sim T/\omega$  behavior of the thermal distribution. Although the distribution is subthermal, the increase in magnon number may be sufficient to drive the system into a disordered state, as indicated by the phase boundary in Fig. 1. This symmetry-breaking phase transition is a nonequilibrium version of the standard equilibrium phase transition driven by raising temperature. Distinct from this transition Walldorf *et al.* also found a change in the magnon distribution from subthermal to superthermal that occurred as the relative drive strength was increased beyond the critical value  $g = 1$  [59]. It is this *subthermal-to-superthermal* transition, which is characterized by a qualitative change in the distribution and is not directly related to the disappearance of a conventional order parameter, that we investigate here. Because the distribution function is at least thermal, in the two-dimensional Heisenberg-symmetry case studied in detail here, long-range order is necessarily destroyed at  $g = 1$ . However, in two-dimensional  $xy$ / $xxz$  systems or in three-dimensional systems, the ordered phase may persist into the superthermal phase.

### B. Nonequilibrium steady state

Figure 2(a) compares the magnon distribution function calculated with and without magnon-magnon scattering. We find that the clear qualitative difference between the subthermal and superthermal cases is still evident in the interacting case, confirming that the nonequilibrium phase transition is preserved under magnon-magnon scattering. In the subthermal steady state, the impact of magnon-magnon scattering is rather small, producing only a slight shift of magnon occupation towards lower frequencies. In striking contrast, the superthermal steady state is strongly affected by magnon-magnon scattering. At all but the lowest frequency the effect

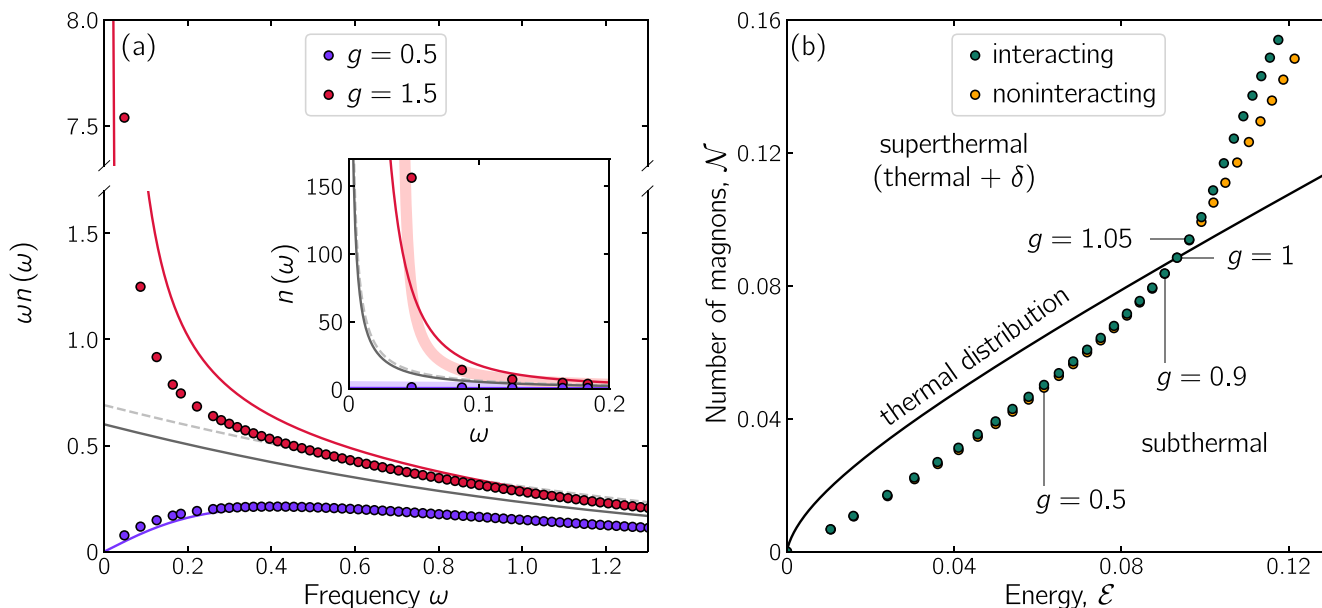


FIG. 2. Nonequilibrium phase transition. (a) Interaction-induced changes in the steady-state magnon occupation  $n(\omega)$ . Plotted is  $\omega n(\omega)$  as a function of magnon frequency  $\omega$  in order to highlight the difference between subthermal [ $\omega n(\omega) \rightarrow 0$  for  $\omega \rightarrow 0$ ], thermal [ $\omega n(\omega) \rightarrow \text{const}$ ], and superthermal [ $\omega n(\omega) \rightarrow \infty$ ] regimes. The blue (red) data points show the interacting results for representative subthermal (superthermal),  $g = 0.5$  ( $g = 1.5$ ), cases in comparison with the noninteracting results shown by blue (red) curves. The dark gray solid line indicates a thermal state at  $g = 1$  and  $T = 0.6$ ; the light gray dashed line is a best fit to the high-frequency part of the interacting distribution function at  $g = 1.5$  and corresponds to a thermal state with an effective temperature  $T > \tilde{T}$ . Inset: The same results plotted as  $n(\omega)$  versus  $\omega$ , focusing on the low-frequency part to highlight that the interacting superthermal system shows a low-frequency divergence that is stronger than both the noninteracting system and the best thermal fit. (b) Points: magnon number vs total energy curve defined from Eq. (4) with  $g$  as an implicit parameter for both noninteracting and interacting steady states. Solid black line: magnon number vs total energy relation obtained from Bose distribution with chemical potential  $\mu = 0$  with temperature as an implicit parameter. States below this critical Bose-Einstein condensation line have a lower number of magnons per energy than a thermal state. States above the critical line have a number of magnons that exceeds the maximal number in states with  $\omega(\mathbf{k}) > 0$  that is compatible with the given system energy in a thermal state, implying the existence of a  $\delta$ -function contribution at zero energy (condensate fraction) in the thermodynamic limit.

of the scattering is to drive the distribution close to a thermal distribution, but the occupancy at the lowest frequency is strongly enhanced relative to the noninteracting case [see inset in Fig. 2(a)].

To interpret our results, we recall equilibrium BEC, in which the occupancy is given by a Bose-Einstein distribution with  $\mu = 0$  and a  $\delta$ -function at  $\omega_k = 0$  describing the condensate fraction. This distribution has a temperature that is fixed by the total energy; the number of uncondensed bosons is then uniquely determined by this temperature, and any excess over the uncondensed number makes up the condensate fraction. With this in mind we plot in Fig. 2(b) the magnon number as a function of magnon energy, with  $g$  being an implicit parameter, along with the magnon number–energy relation implied by the Bose distribution with chemical potential  $\mu = 0$  and no condensate, with temperature being an implicit parameter. In ordinary BEC, decreasing the temperature decreases the energy moving the system to the left along a line at fixed  $\mathcal{N}$ . Crossing the solid line signals the BEC. In our system for  $g < 1$  the number-energy trace remains below the solid line. At  $g = 1$  the curves for both noninteracting and interacting systems cross the solid line, implying for  $g > 1$  an excess of magnons. Importantly, magnon-magnon interactions push the system even farther away from the thermal distribution rather than towards it because magnon-magnon scattering tends to redistribute magnons towards lower energy, thus

accommodating more magnons per energy compared to the noninteracting steady state.

### C. Finite-size scaling analysis

To further interpret the data we present a finite-size scaling analysis. We define the magnon occupancy at the  $m$ th frequency weighted by the discretized density of states,  $\mathcal{N}_m = \rho(\omega_m)n(\omega_m)$ . Figures 3(a) and 3(b) strongly suggest that the occupancy  $\mathcal{N}_0$  of the lowest-frequency magnon mode remains a nonvanishing fraction of the overall number of magnons  $\mathcal{N}$  as the system size increases in any interacting system with  $g > 1$ . This is different from the case  $g = 1$ , which has no condensate and where the contribution of the lowest frequency vanishes as the system size increases. Figures 3(c) and 3(d) show that the ratio of the occupancy at the second-smallest frequency to the occupancy at the smallest frequency  $\mathcal{N}_1/\mathcal{N}_0$  decreases as the system size increases. The decrease is apparently linear in  $1/\ell$ , but the system sizes available are not sufficient to allow for a precise determination. The combination of a nonvanishing  $\mathcal{N}_0/\mathcal{N}$  and a vanishing  $\mathcal{N}_1/\mathcal{N}_0$  in the thermodynamic limit strongly suggests the existence of a  $\delta$ -function contribution at  $\omega = 0$ . For reference, we also show data points for a system that is initialized with the noninteracting steady state at a given value of  $g$  and then evolved as a closed system under magnon-magnon scattering.

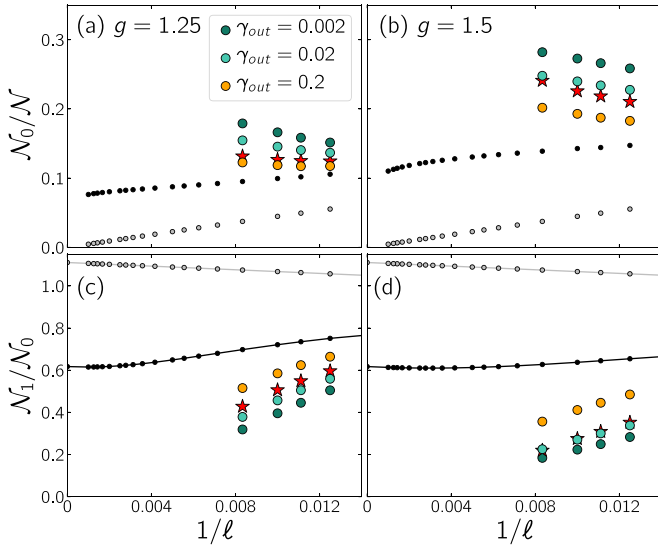


FIG. 3. Finite-size scaling analysis revealing the  $\delta$ -function contribution at  $g > 1$  in the thermodynamic limit. (a) and (b) Ratio of the magnon density at the lowest frequency and the total number of magnons in the system  $\mathcal{N}_0/\mathcal{N}$  and (c) and (d) ratio of the magnon density at the second-lowest frequency and the lowest frequency  $\mathcal{N}_1/\mathcal{N}_0$  for  $g = 1.25$  (left panels) and  $g = 1.5$  (right panels). Different colors correspond to different values of  $\gamma_{\text{out}} = 0.002, 0.02, 0.2$  as indicated. Black points correspond to the noninteracting stationary state, gray points show thermal behavior ( $g = 1$ ), and red stars correspond to the stationary state to which the interacting, closed system evolves when initialized with the respective noninteracting stationary state at given  $g$ .

At  $g > 1$  this closed system is positioned above the critical line for BEC in the  $\mathcal{N}$ - $\mathcal{E}$  diagram in Fig. 2(b). Therefore, in the thermodynamic limit this closed system necessarily develops a finite condensate fraction because this is the only possible thermalized solution to the closed-system kinetic equation. The comparison between the interacting driven-dissipative steady states and the closed-system thermalized states drives home our point that the interacting  $g > 1$  system develops a nonvanishing condensate fraction in the thermodynamic limit [61].

#### D. Static and dynamic criticality

Figure 4 examines the nature of static and dynamic criticality occurring as  $g$  is tuned through  $g = 1$ . The main panels show both the dependence of the static observable  $d\mathcal{N}/dg$  [Fig. 4(a)] and the dynamic decay rate  $\lambda_{\mathcal{N}}$  [Fig. 4(b)], as defined by

$$\mathcal{N}(t) = \mathcal{N}_{\text{final}} + \Delta\mathcal{N} \exp(-\lambda_{\mathcal{N}}t) \quad (6)$$

on the tuning parameter  $g$ . Equation (6) is the empirically observed long-time behavior of the excitation density in the system [62]. Data are shown for different system sizes. For both quantities there is a clear difference between  $g < 1$  and  $g > 1$  with weak system-size dependence for  $g < 1$  and strong system-size dependence for  $g > 1$ . The insets in Fig. 4(a) and (b) show approximate data collapses that are consistent

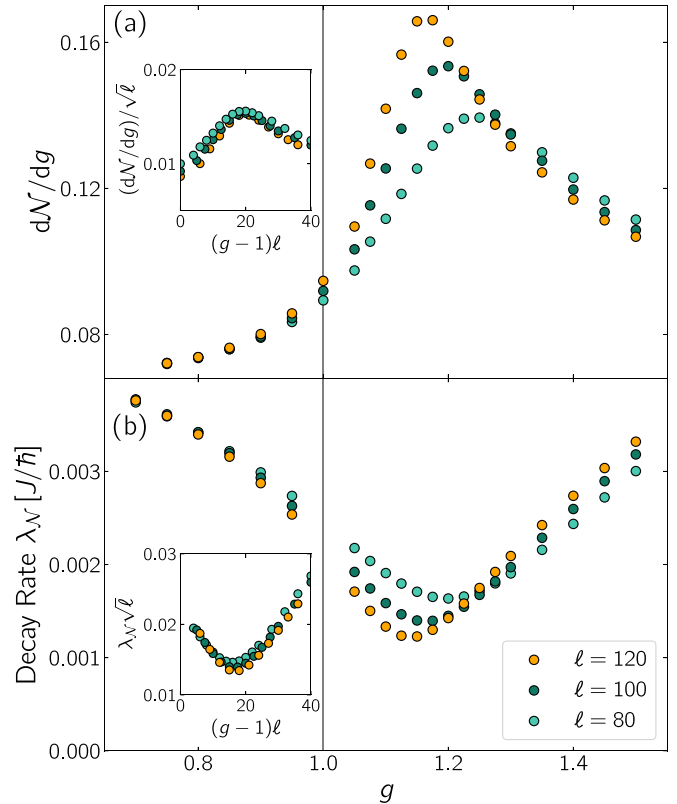


FIG. 4. Static and dynamical critical behavior in the interacting driven-dissipative steady state. (a) Rate of change of magnon number  $\mathcal{N}$  as a function of  $g$ . Inset: Scaling behavior with the linear system size collapses the data points onto a single curve. (b) Rate of decay of total magnon number  $\mathcal{N}$  towards the stationary state, plotted as a function of  $g$  for different system sizes as indicated. Inset: Scaling behavior with the linear system size is consistent with collapse onto a single curve, suggesting critical slowing down as  $g \rightarrow 1$ . (For critical behavior in the strength of the condensate fraction, see Appendix B.)

with critical scaling as  $g \rightarrow 1$  from above and  $\ell \rightarrow \infty$ . The implication of the data collapse is that

$$\frac{d\mathcal{N}}{dg} = f_1[(g-1)\ell] \sqrt{\ell}, \quad (7a)$$

$$\lambda_{\mathcal{N}} = \frac{f_2[(g-1)\ell]}{\sqrt{\ell}}. \quad (7b)$$

If  $d\mathcal{N}/dg$  and  $\lambda_{\mathcal{N}}$  are to be finite and nonzero as  $\ell \rightarrow \infty$ , functions  $f_1(x)$  and  $f_2(x)$  need to have the forms  $f_1(x) \propto (1/\sqrt{x})$  and  $f_2(x) \propto \sqrt{x}$  as  $x \rightarrow \infty$ , implying that at  $\ell = \infty$ ,  $d\mathcal{N}/dg \sim \frac{1}{\sqrt{g-1}}$ , i.e., a square-root singularity of  $\mathcal{N}(g)$  in the thermodynamic limit, and  $\lambda_{\mathcal{N}} \sim \sqrt{g-1}$  as  $g \rightarrow 1^+$ , i.e., a critical slowing down as  $g \rightarrow 1$  from above. This asymmetric criticality is not present in the noninteracting theory and is a consequence of magnon-magnon interactions.

#### IV. DISCUSSION

A driven-dissipative system may exhibit two phase transitions as a function of drive strength. One is the nonequilibrium analog of a conventional symmetry-breaking transition that

occurs because the drive creates excitations which push the system away from the ordered state. This transition was previously studied [8,10,12–15,42,43]. The other type, studied here, is that when the drive exceeds a critical value set by the linear dissipation mechanism, a kind of “order from disorder” transition may occur, with some fraction of the drive-induced excitations condensing into a zero-momentum ground state. Our finding bears an interesting relationship to the existing literature on Bose-Einstein condensation of magnons, where an evolution into a condensed state of a transiently induced magnon population is analyzed.

Crucial to our analysis is a numerically exact solution of the Boltzmann equation derived by considering the interactions among excitations, which enables an analysis of the interplay between the frequency dependence of the dissipation mechanism and the tendency to condensation. This comprehensive numerical solution extends previously published theory which typically uses either a phenomenological relaxation rate or a simple approximation to the magnon-magnon scattering term. A key finding is that the condensation occurs in a high-drive limit, where the drive-induced energy density is large and the number of excited magnons is also large, and is associated with a dynamical (drive-strength-driven) criticality. On the level of theory used here, this criticality is described by a different set of static and dynamic critical exponents.

Our work raises many important questions. First, while we have demonstrated a qualitative change in the magnon distribution consistent with the formation of a condensate, the physics of fluctuations around this state has not yet been studied, and therefore, a full analysis of the criticality, beyond the Boltzmann approximation used here, cannot be undertaken. Important open problems include understanding how to characterize the differences between the nonthermal symmetry-breaking transition and the usual thermal one, how to interpret transitions involving distribution functions and not conventional order parameters, and how to generalize the standard equilibrium theory of spatial and temporal fluctuations in a critical state to strongly nonequilibrium situations such as that considered here. The issues are of particular importance in two dimensions, where the obvious generalization of the Hohenberg-Mermin-Wagner theorem to nonequilibrium situations would suggest that the Bose-Einstein condensation we find signals a phase with power law correlations.

Observation of the nonthermal critical behavior predicted here is an important experimental challenge. Possible techniques include time-resolved second harmonic optical polarimetry and inelastic x-ray scattering [63]. Our work also has a close connection to Bose-Einstein condensation in exciton-polariton systems, for which interesting field-theory-based studies of criticality have appeared [42,43]. Investigations of possible nonequilibrium-induced spatial structure, analogous to the structures observed in turbulence

[64], and clarifying the relation of our work to nonthermal fixed points in closed systems after quenches [65–67] are also important directions for future research.

## ACKNOWLEDGMENTS

We acknowledge discussions with S. Diehl and M. Mirano. This work was supported by the Max Planck–New York City Center for Nonequilibrium Quantum Phenomena. M.A.S. acknowledges financial support through the Deutsche Forschungsgemeinschaft (DFG, German Research Foundation) via the Emmy Noether program (SE 2558/2). D.M.K. acknowledges support from the Deutsche Forschungsgemeinschaft (DFG, German Research Foundation) via RTG 1995 and Germany’s Excellence Strategy – Cluster of Excellence Matter and Light for Quantum Computing (ML4Q) EXC 2004/1 – 390534769. A.J.M. is supported in part by Programmable Quantum Materials, an Energy Frontier Research Center funded by the U.S. Department of Energy (DOE), Office of Science, Basic Energy Sciences (BES), under Award No. DE-SC0019443. The Flatiron Institute is a division of the Simons Foundation.

## APPENDIX A: METHODS

*Interacting spin-wave theory.* We consider the isotropic Heisenberg antiferromagnet as given in Eq. (1) and apply standard Holstein-Primakoff spin-wave theory [58], resulting in

$$H_{\text{HP}} = E_0 + H_0 + V, \quad (\text{A1})$$

with an irrelevant ground state energy  $E_0$  and bilinear Hamiltonian

$$H_0 = \sum_k \hbar \omega_k (\alpha_k^\dagger \alpha_k + \beta_k^\dagger \beta_k). \quad (\text{A2})$$

The magnon dispersion is

$$\omega_k = \frac{JS_z}{\hbar} \left[ 1 + \frac{1}{2S} \left( 1 - \frac{2}{N} \sum_{k'} \lambda_{k'} \right) \right] \lambda_k, \quad (\text{A3})$$

with

$$\lambda_k = \sqrt{1 - \gamma_k^2}, \quad (\text{A4a})$$

$$\gamma_k = \frac{\cos(k_x) + \cos(k_y)}{2}. \quad (\text{A4b})$$

The interaction term for the kinematically allowed magnon energy and momentum conserving scattering processes is given by  $V$  with interaction vertices  $V_{1_\alpha^+ 2_\alpha^+ 3_\alpha^- 4_\alpha^-}^{(2;2)}$  and  $\tilde{V}_{1_\alpha^+ 2_\beta^+ 3_\alpha^- 4_\beta^+}^{(2;2)}$ , namely,

$$V = -J \frac{2z}{N} \sum_{\mathbf{k}_1 \mathbf{k}_2 \mathbf{k}_3 \mathbf{k}_4} \delta(\mathbf{k}_1 + \mathbf{k}_2 - \mathbf{k}_3 - \mathbf{k}_4) \{ V^{(2;2)} (\alpha_1^\dagger \alpha_2^\dagger \alpha_3 \alpha_4 + \beta_3^\dagger \beta_4^\dagger \beta_1 \beta_2) + \tilde{V}^{(2;2)} (\alpha_1^\dagger \alpha_3 \beta_4^\dagger \beta_2) \}, \quad (\text{A5a})$$

$$V_{1_\alpha^+ 2_\alpha^+ 3_\alpha^- 4_\alpha^-}^{(2;2)} = \gamma_{(2-4)} u_1 u_3 v_2 v_4 + \frac{1}{4} [\gamma_1 u_1 v_2 v_3 v_4 + \gamma_2 u_1 u_3 u_4 v_2 + \gamma_3 u_3 v_1 v_2 v_4 + \gamma_4 u_1 u_2 u_3 v_4], \quad (\text{A5b})$$

$$\tilde{V}_{1_\alpha^+ 2_\beta^+ 3_\alpha^- 4_\beta^+}^{(2;2)} = \gamma_{(2-4)} [u_1 u_2 u_3 u_4 + v_1 v_2 v_3 v_4] + \gamma_{(2-3)} [u_1 u_2 v_3 v_4 + u_3 u_4 v_1 v_2]$$

$$\begin{aligned}
 & + \frac{1}{2} \gamma_1 [u_3 v_1 v_2 v_4 + u_1 u_2 u_4 v_3] + \frac{1}{2} \gamma_2 [u_1 u_2 u_3 v_4 + u_4 v_1 v_2 v_3] \\
 & + \frac{1}{2} \gamma_3 [u_2 u_3 u_4 v_1 + u_1 v_2 v_3 v_4] + \frac{1}{2} \gamma_4 [u_2 v_1 v_3 v_4 + u_1 u_3 u_4 v_2].
 \end{aligned} \tag{A5c}$$

Here, we have used

$$u_k = \sqrt{\frac{1 + \lambda_k}{2\lambda_k}}, \tag{A6a}$$

$$v_k = -\text{sign}(\gamma_k) \sqrt{\frac{1 - \lambda_k}{2\lambda_k}}. \tag{A6b}$$

In Eq. (A5a), the momentum-conserving  $\delta$ -function should be understood as modulo a reciprocal lattice vector of the standard two-dimensional antiferromagnetic Brillouin zone.

$$\begin{aligned}
 \mathcal{S}_\alpha^{(2;2)}(\mathbf{k}_1) &= \sum_{\mathbf{k}_2 \mathbf{k}_3 \mathbf{k}_4} \delta(\mathbf{k}_1 + \mathbf{k}_2 - \mathbf{k}_3 - \mathbf{k}_4) \delta(\omega_{\mathbf{k}_1} + \omega_{\mathbf{k}_2} - \omega_{\mathbf{k}_3} - \omega_{\mathbf{k}_4}) \mathcal{V}_{1_\alpha^+ 2_\alpha^+ 3_\alpha^- 4_\alpha^-}^{(2;2)} \mathcal{V}_{3_\alpha^+ 4_\alpha^+ 1_\alpha^- 2_\alpha^-}^{(2;2)} \\
 &\times \{ [1 + n^\alpha(\mathbf{k}_1)] [1 + n^\alpha(\mathbf{k}_2)] n^\alpha(\mathbf{k}_3) n^\alpha(\mathbf{k}_4) - n^\alpha(\mathbf{k}_1) n^\alpha(\mathbf{k}_2) [1 + n^\alpha(\mathbf{k}_3)] [1 + n^\alpha(\mathbf{k}_4)] \},
 \end{aligned} \tag{A8}$$

$$\begin{aligned}
 \tilde{\mathcal{S}}_\alpha^{(2;2)}(\mathbf{k}_1) &= \sum_{\mathbf{k}_2 \mathbf{k}_3 \mathbf{k}_4} \delta(\mathbf{k}_1 + \mathbf{k}_2 - \mathbf{k}_3 - \mathbf{k}_4) \delta(\omega_{\mathbf{k}_1} + \omega_{\mathbf{k}_2} - \omega_{\mathbf{k}_3} - \omega_{\mathbf{k}_4}) \tilde{\mathcal{V}}_{1_\alpha^+ 2_\beta^- 3_\alpha^- 4_\beta^+}^{(2;2)} \tilde{\mathcal{V}}_{3_\alpha^+ 4_\beta^- 1_\alpha^- 2_\beta^+}^{(2;2)} \\
 &\times \{ [1 + n^\alpha(\mathbf{k}_1)] [1 + n^\beta(\mathbf{k}_4)] n^\alpha(\mathbf{k}_3) n^\beta(\mathbf{k}_2) - n^\alpha(\mathbf{k}_3) n^\beta(\mathbf{k}_2) [1 + n^\alpha(\mathbf{k}_1)] [1 + n^\beta(\mathbf{k}_4)] \}.
 \end{aligned} \tag{A9}$$

*Computational remarks.* We compute the time evolution on the two-dimensional antiferromagnetic Brillouin zone, which is discretized into square tiles and subsequently mapped onto an energy grid (see Appendix D for details). The time propagation of the full kinetic equation in the main text is performed using the two-step Adams-Bashforth method. We have carefully checked convergence in the time step discretization.

The staggered magnetization is computed via

$$m(S, n(\omega)) = S + \frac{1}{2} - \omega_{\max} \sum_{m=1}^{\omega_{\max}} \frac{\rho(\omega_m)}{\omega_m} \left( n(\omega_m) + \frac{1}{2} \right). \tag{A10}$$

Specifically, the black curve in Fig. 1 that separates the subthermal disordered phase from the subthermal ordered phase is computed by solving the equation  $m(S, n(\omega)) = 0$  (with the noninteracting magnon distribution at a given  $g$  inserted to compute  $m$ ) for  $1/S$ .

### APPENDIX B: STRENGTH OF THE CONDENSATE FRACTION

The strength of the condensate fraction is determined by the ratio of the number of magnons  $\mathcal{N}$  to the system energy  $\mathcal{E}$ . Projecting each individual point in Fig. 2(b) vertically onto the thermal distribution gives the number of magnons  $\mathcal{N}_{\text{th}}$  that can be accommodated by the thermal distribution. The excess of magnons determines the strength of the  $\delta$ -function,  $\mathcal{D}_0 \equiv$

*Boltzmann equation.* The semiclassical magnon Boltzmann equation for the magnon distribution in branch  $\alpha$  at a given momentum  $\mathbf{k}_1$  is

$$\frac{dn^\alpha(\mathbf{k}_1)}{dt} = \frac{2\pi}{\hbar} \left( \frac{2Jz}{N} \right)^2 [S_\alpha^{(2;2)}(\mathbf{k}_1) + \tilde{S}_\alpha^{(2;2)}(\mathbf{k}_1)], \tag{A7}$$

where  $S$  are the relevant scattering integrals. To leading order in  $1/S$ , only scattering processes with two magnons scattering into two other magnons are kinematically allowed. Consequently, the scattering conserves the number of magnons term by term at this level of approximation. The corresponding scattering integrals are given by

$\mathcal{N} - \mathcal{N}_{\text{th}}$ . Therefore the steady state has the form

$$\mathcal{N}(\omega) = \mathcal{D}_0 \mathcal{N}_\Delta(\omega) + \mathcal{N}_{\text{th}, T_\varepsilon}(\omega), \tag{B1}$$

where  $\mathcal{N}_\Delta(\omega)$  is a normalized function (integrating to unity) and, as discussed above, turns into a  $\delta$  function in the thermodynamic limit. Since the number of magnons exceeds only the number of magnons in a thermal distribution at  $g > 1$ , the

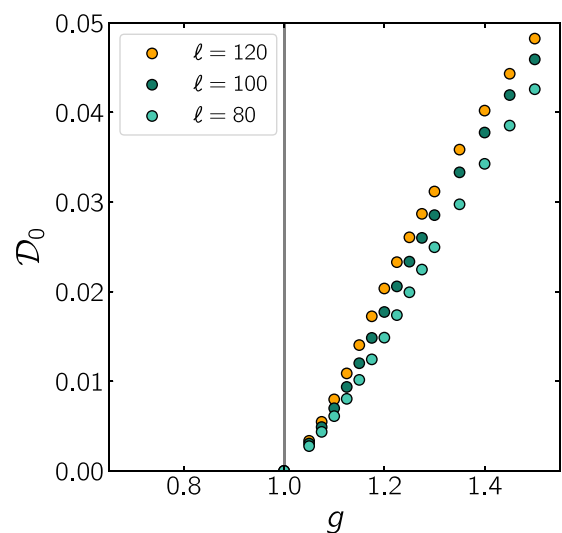


FIG. 5. Condensate fraction  $\mathcal{D}_0$  as a function of the dimensionless tuning parameter  $g$  for different linear system sizes as indicated.

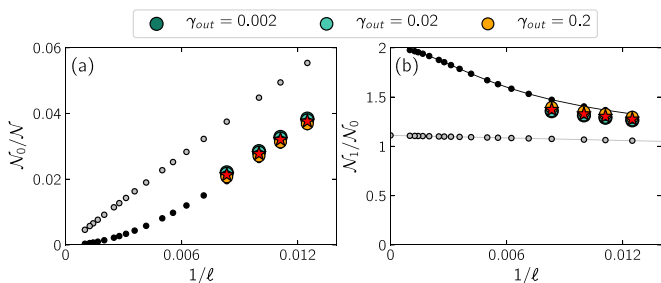


FIG. 6. Finite-size scaling analysis analogous to Fig. 4 for the subthermal regime ( $g = 0.875$ ). (a) Ratio of the magnon density at the lowest frequency and the total number of magnons in the system  $\mathcal{N}_0/\mathcal{N}$  and (b) ratio of the magnon density at the second-lowest frequency and the lowest frequency  $\mathcal{N}_1/\mathcal{N}_0$ . Different colors correspond to different values of  $\gamma_{\text{out}} = 0.002, 0.02, 0.2$  as indicated. Black points correspond to the noninteracting stationary state, gray points show thermal behavior ( $g = 1$ ), and red stars correspond to the stationary state to which the interacting, closed system evolves when initialized with the respective noninteracting stationary state at given  $g$ .

weight of the  $\delta$ -function  $\mathcal{D}_0$  vanishes for  $g < 1$ . The decrease in the weight of the  $\delta$ -function  $\mathcal{D}_0$  to zero at  $g = 1$  marks the phase transition (Fig. 5).

**APPENDIX C: SCALING OF THE MAGNON NUMBER IN THE LIMIT OF WEAK DRIVING**

In the low-driving phase  $g < 1$  the scaling behavior is substantially different from the results in the strong-driving phase. This is visible in Fig. 6(a), where the contribution of the lowest frequency in the interacting phase goes to zero as system size is increased, just as in the thermal system. So at  $g < 1$  there are no indications for a condensate fraction at  $\omega = 0$ . Similarly, there is only a minimal shift from the noninteracting results in the ratio of the magnon density at the second-lowest frequency and the lowest frequency  $\mathcal{N}_1/\mathcal{N}_0$ . This behavior in the low-driving ordered phase is substantially different from the findings in the high-driving, disordered phase.

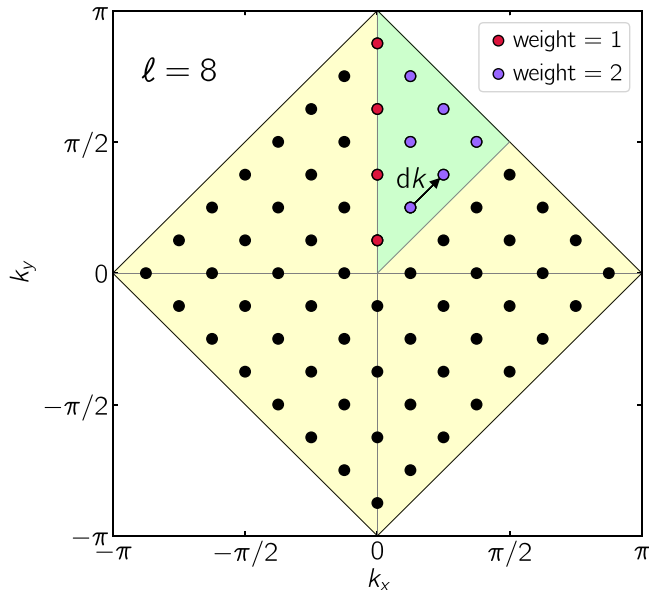


FIG. 7. Magnetic Brillouin zone (MBZ) for  $\ell = 8$ . The full MBZ (yellow) can be reduced to  $(\ell^2 + 2\ell)/8$  lattice sites (green) due to the symmetry of the lattice. The multiplicity weights of the reduced lattice vectors that are sufficient to simulate the dynamics in the system are marked as indicated.

**APPENDIX D: PSEUDOCODE**

We numerically consider a quadratic lattice of momentum vectors as displayed in Fig 7 with linear dimension  $\ell$  and  $\ell^2$  lattice sites. To make our computation numerically feasible even for comparatively large  $\ell$  we then reduce this magnetic Brillouin zone (MBZ) using symmetry relations to  $(\ell^2 + 2\ell)/8$  lattice sites (green). These reduced MBZ vectors  $k_{\text{PZ}}$  are associated with different weights due to their multiplicity, as indicated. Please note that in the following pseudocode # denotes the number of a quantity in an array, while symbols like  $k_{\text{PZ}}$  without a # are the actual quantity. For example,  $k_{\text{PZ}}$  without a # is the actual vector in the reduced MBZ.

1. Building the full (yellow) and reduced (green) MBZs as displayed in Fig. 7.

```

1: Save MBZ vectors sorted by length in MBZ[#k_MBZ][k_x, k_y]
2: Save vectors within the reduced MBZ sorted by length in PZ[#k_PZ][k_x, k_y]
3: for k in PZ do
4:   save the precise energy associated with this vector as Omega[#k_PZ]
5:   save the weight associated with this vector as kweight[#k_PZ]
6: end for
    
```

The scattering conserves both momentum and energy. This is implemented numerically by mapping the MBZ in momentum space on an energy grid as displayed in Fig. 8. To do so, we divide the interval  $\{0, \Omega_{\text{max}}\}$  into  $\ell$  equidistant energy bins and determine with which bin the vectors in the momentum grid are associated. The different colors of the bins in Fig. 8 are simply to distinguish them from each other and have no further meaning. Since not all bins will have energies, not all bins need to be taken into account. Note that in the example of  $\ell = 8$  only five of the bins are occupied (purple  $\omega$ ). Each bin is then associated with the total weight of the MBZ vectors in it (red numbers).

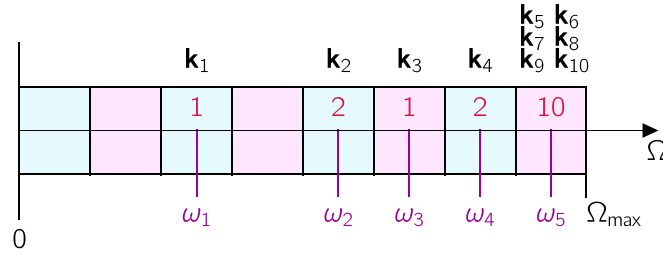


FIG. 8. Mapping of the momentum grid onto an energy grid for  $\ell = 8$ . The interval  $\{0, \Omega_{\max}\}$  into  $\ell$  equidistant energy bins (blue and magenta) and for each momentum vector  $\mathbf{k}_{\text{PZ}}$  of the associated bin is determined. The red numbers give the total weight of all vectors within the energy bin, so, for example, energy bin  $\omega_5$  has momentum vectors  $\{\mathbf{k}_5, \mathbf{k}_6, \mathbf{k}_7, \mathbf{k}_8, \mathbf{k}_9, \mathbf{k}_{10}\}$ , which have a total weight of 10.

## 2. Map the reduced MBZ in $\mathbf{k}$ space onto an energy grid as illustrated in Fig. 8.

- 
- 1: Divide the interval  $\{0, \Omega_{\max}\}$  into  $\ell$  equidistant energy bins (see Fig. 8, blue and magenta boxes)
  - 2: **for**  $k \in \text{PZ}$
  - 3:   identify in which energy bin  $\Omega[\#k]$  falls
  - 4: **end for**
  - 5: Discard empty energy bins
  - 6: Save the center of the remaining energy bins as energybin[# $\omega$ ]  
(see purple  $\{\omega_1, \omega_2, \omega_3, \omega_4, \omega_5\}$  in Fig. 8)
  - 7: Save the numbers of reduced MBZ vectors in each bin as kpz@energybin[# $\omega$ ][#k<sub>PZ</sub>]
  - 8: Compute the total kweight in each bin and save it as kweight@energybin[# $\omega$ ][#k<sub>PZ</sub>]
- 

The next step is to find the quadruples in momentum space that satisfy momentum and energy conservation simultaneously. Note that we use the centers of the energy bins and not the precise energies of the momentum vectors to determine whether energy conservation is satisfied. The factor of 4 in the cutoff is needed because each quadruple consists of four momentum vectors. Furthermore, all entries of the two-dimensional array “integrals” are the same. Here, the cutoff has to be divided by  $\ell^4$  because there are four free dimensions in the integration. The vertices are then symmetrized by computing

$$(\mathcal{V}\mathcal{V})_{\text{sym}} = 0.125[\mathcal{V}_{1\alpha^+2\alpha^+3\alpha^-4\alpha^-} + \mathcal{V}_{3\alpha^+4\alpha^+1\alpha^-2\alpha^-}] + 0.125[\mathcal{V}_{1\alpha^+2\alpha^+4\alpha^-3\alpha^-} + \mathcal{V}_{3\alpha^+4\alpha^+2\alpha^-1\alpha^-}] + 0.125[\mathcal{V}_{2\alpha^+1\alpha^+3\alpha^-4\alpha^-} + \mathcal{V}_{4\alpha^+3\alpha^+1\alpha^-2\alpha^-}] + 0.125[\mathcal{V}_{2\alpha^+1\alpha^+4\alpha^-3\alpha^-} + \mathcal{V}_{4\alpha^+3\alpha^+2\alpha^-1\alpha^-}] \quad (\text{D1})$$

and

$$(\tilde{\mathcal{V}}\tilde{\mathcal{V}})_{\text{sym}} = 0.25[\tilde{\mathcal{V}}_{1\alpha^+4\beta^-3\alpha^-2\beta^+} + \tilde{\mathcal{V}}_{3\alpha^+2\beta^-1\alpha^-4\beta^+}] + 0.25[\tilde{\mathcal{V}}_{2\alpha^+3\beta^-4\alpha^-1\beta^+} + \tilde{\mathcal{V}}_{4\alpha^+1\beta^-2\alpha^-3\beta^+}]. \quad (\text{D2})$$

This vertex symmetrization ensures energy and particle number conservation by enforcing detailed balance and is a necessary step in the energy-grid representation.

## 3. Find quadruples that satisfy momentum and energy conservation in momentum space.

- 
- 1: cutoff =  $4 * \Omega_{\max} / \ell$
  - 2: **for**  $k_1 \in \text{PZ}$  **do**
  - 3:   **for**  $k_2 \in \text{MBZ}$  **do**
  - 4:     **for**  $k_3 \in \text{MBZ}$  **do**
  - 5:        $k_4 = k_1 + k_2 - k_3$
  - 6:       Find bin energy  $\omega_i$  associated with each of  $\{k_1, k_2, k_3, k_4\} \rightarrow \{\omega_1, \omega_2, \omega_3, \omega_4\}$
  - 7:       **if**  $\omega_1 + \omega_2 - \omega_3 - \omega_4 < 0.05 * \text{cutoff}$  **then**
  - 8:         Save quadruple as kquadruple[#k1][#quadruple][ $\{k_1, k_2, k_3, k_4\}$ ]
  - 9:         Compute  $(\mathcal{V}\mathcal{V})_{\text{sym}} = (\text{symmetrize}[\mathcal{V}_{1\alpha^+2\alpha^+3\alpha^-4\alpha^-}])^2$
  - 10:        Compute  $(\tilde{\mathcal{V}}\tilde{\mathcal{V}})_{\text{sym}} = (\text{symmetrize}[\tilde{\mathcal{V}}_{1\alpha^+2\beta^-3\alpha^-4\beta^+}])^2$
  - 11:        Set vertices[#k1][#quadruple] =  $\mathcal{V}\mathcal{V}_{\text{sym}} + \tilde{\mathcal{V}}\tilde{\mathcal{V}}_{\text{sym}}$
  - 12:        Set integrals[#k1][#quadruple] = cutoff/ $(\ell^4)$
  - 13:        **end if**
  - 14:     **end for**
  - 15:    **end for**
  - 16: **end for**
-

Now we have found the quadruples in momentum space, but in order to compute the time evolution using the energy grid in Fig. 8 we need to turn the quadruple list into an energy list with  $\omega_1, \omega_2, \omega_3,$  and  $\omega_4$  and then average for each given  $\omega_1$  over the multiple entries. This gives a consolidated list of energy quadruples and their weights.

#### 4. Convert momentum quadruples into energy quadruples.

---

```

1: for  $\omega \in \text{energybins}$  do
2:   for  $k \in \text{kweight@energybin}[\#\omega]$  do
3:     for  $q \in \text{kquadruple}[\#k]$  do
4:        $\{k_1, k_2, k_3, k_4\} = \text{kquadruple}[\#k][\#q]$ 
5:       Find energy bins associated with  $k_1, k_2, k_3,$  and  $k_4 \rightarrow \{\omega_1, \omega_2, \omega_3, \omega_4\}$ 
6:       Safe energyquadruples $[\#\omega][\#equadruple][\{\omega_1, \omega_2, \omega_3, \omega_4\}]$ 
7:       energyweight = integrals $[\#k][\#q] * \text{vertices}[\#k][\#q] * \text{kweight}[\#k]$ 
8:       Set energyweights $[\#\omega][\#equadruple] = \text{energyweight}$ 
9:     end for
10:   end for
11:   for equad  $\in \text{energyquadruples}[\#\omega]$  do
12:     Check if the combination  $\{\omega_1, \omega_2, \omega_3, \omega_4\}$  has already been found
13:     if No then
14:       Save energyquadruples_consolidated $[\#\omega][\#equad\_c][\{\omega_1, \omega_2, \omega_3, \omega_4\}]$ 
15:       energyweight_averaged = energyweights $[\#\omega]/\text{kweight@energybin}[\#\omega]$ 
16:       Save energyweights_consolidated $[\#\omega][\#equad\_c] = \text{energyweight\_averaged}$ 
17:     else if Yes then
18:       energyweight_averaged = energyweights $[\#\omega]/\text{kweight@energybin}[\#\omega]$ 
19:       Add energyweights_consolidated $[\#\omega][\#equad\_c]+ = \text{energyweight\_averaged}$ 
20:     end for
21:   end for
22: end for

```

---

We then use the consolidated quadruples in energy space to compute the time evolution using the two-step Adams-Bashforth linear multistep method.

- 
- [1] D. N. Basov, R. D. Averitt, and D. Hsieh, Towards properties on demand in quantum materials, *Nat. Mater.* **16**, 1077 (2017).
  - [2] A. de la Torre, D. M. Kennes, M. Claassen, S. Gerber, J. W. McIver, and M. A. Sentef, Colloquium: Nonthermal pathways to ultrafast control in quantum materials, *Rev. Mod. Phys.* **93**, 041002 (2021).
  - [3] N. Tsuji, M. Eckstein, and P. Werner, Nonthermal Antiferromagnetic Order and Nonequilibrium Criticality in the Hubbard Model, *Phys. Rev. Lett.* **110**, 136404 (2013).
  - [4] J. Klinder, H. Keßler, M. Wolke, L. Mathey, and A. Hemmerich, Dynamical phase transition in the open Dicke model, *Proc. Natl. Acad. Sci. USA* **112**, 3290 (2015).
  - [5] A. F. Kemper, O. Abdurazakov, and J. K. Freericks, General Principles for the Nonequilibrium Relaxation of Populations in Quantum Materials, *Phys. Rev. X* **8**, 041009 (2018).
  - [6] M. Yarmohammadi, C. Meyer, B. Fauseweh, B. Normand, and G. S. Uhrig, Dynamical properties of a driven dissipative dimerized  $S = \frac{1}{2}$  chain, *Phys. Rev. B* **103**, 045132 (2021).
  - [7] M. F. Maghrebi and A. V. Gorshkov, Nonequilibrium many-body steady states via Keldysh formalism, *Phys. Rev. B* **93**, 014307 (2016).
  - [8] A. Mitra, S. Takei, Y. B. Kim, and A. J. Millis, Nonequilibrium Quantum Criticality in Open Electronic Systems, *Phys. Rev. Lett.* **97**, 236808 (2006).
  - [9] A. Mitra and A. J. Millis, Coulomb gas on the Keldysh contour: Anderson-Yuval-Hamann representation of the nonequilibrium two-level system, *Phys. Rev. B* **76**, 085342 (2007).
  - [10] A. Mitra and A. J. Millis, Current-driven quantum criticality in itinerant electron ferromagnets, *Phys. Rev. B* **77**, 220404(R) (2008).
  - [11] A. Mitra and A. J. Millis, Current-driven defect-unbinding transition in an XY ferromagnet, *Phys. Rev. B* **84**, 054458 (2011).
  - [12] F. Brennecke, R. Mottl, K. Baumann, R. Landig, T. Donner, and T. Esslinger Real-time observation of fluctuations at the driven-dissipative Dicke phase transition, *Proc. Natl. Acad. Sci. USA* **110**, 11763 (2013).
  - [13] R. Rota, F. Minganti, C. Ciuti, and V. Savona, Quantum Critical Regime in a Quadratically Driven Nonlinear Photonic Lattice, *Phys. Rev. Lett.* **122**, 110405 (2019).
  - [14] C. Klöckner, C. Karrasch, and D. M. Kennes, Nonequilibrium Properties of Berezinskii-Kosterlitz-Thouless Phase Transitions, *Phys. Rev. Lett.* **125**, 147601 (2020).
  - [15] J. Marino and S. Diehl, Driven Markovian Quantum Criticality, *Phys. Rev. Lett.* **116**, 070407 (2016).
  - [16] A. Barman, G. Gubbiotti, S. Ladak, A. O. Adeyeye, M. Krawczyk, J. Gräfe, C. Adelman, S. Cotofana, A. Naemi, V. I. Vasyuchka, B. Hillebrands, S. A. Nikitov *et al.*, The 2021 magnonics roadmap, *J. Phys.: Condens. Matter* **33**, 413001 (2021).

- [17] S. O. Demokritov *et al.*, Bose-Einstein condensation of quasi-equilibrium magnons at room temperature under pumping, *Nature (London)* **443**, 430 (2006).
- [18] D. A. Bozhko *et al.*, Supercurrent in a room-temperature Bose-Einstein magnon condensate, *Nat. Phys.* **12**, 1057 (2016).
- [19] P. Nowik-Boltyk, O. Dzyapko, V. E. Demidov, N. G. Berloff, and S. O. Demokritov, Spatially non-uniform ground state and quantized vortices in a two-component Bose-Einstein condensate of magnons, *Sci. Rep.* **2**, 482 (2012).
- [20] S. A. Bender, R. A. Duine, A. Brataas, and Y. Tserkovnyak, Dynamic phase diagram of dc-pumped magnon condensates, *Phys. Rev. B* **90**, 094409 (2014).
- [21] P. Clausen, D. A. Bozhko, V. I. Vasyuchka, B. Hillebrands, G. A. Melkov, and A. A. Serga, Stimulated thermalization of a parametrically driven magnon gas as a prerequisite for Bose-Einstein magnon condensation, *Phys. Rev. B* **91**, 220402(R) (2015).
- [22] V. E. Demidov, O. Dzyapko, M. Buchmeier, T. Stockhoff, G. Schmitz, G. A. Melkov, and S. O. Demokritov, Magnon Kinetics and Bose-Einstein Condensation Studied in Phase Space, *Phys. Rev. Lett.* **101**, 257201 (2008).
- [23] A. A. Serga, A. V. Chumak, and B. Hillebrands, YIG magnonics, *J. Phys. D* **43**, 264002 (2010).
- [24] A. J. E. Kreil, H. Yu. Musiienko-Shmarova, S. Eggert, A. A. Serga, B. Hillebrands, D. A. Bozhko, A. Pomyalov, and V. S. L'vov, Tunable space-time crystal in room-temperature magnetodielectrics, *Phys. Rev. B* **100**, 020406(R) (2019).
- [25] C. Sun, T. Nattermann, and V. L. Pokrovsky, Bose-Einstein condensation and superfluidity of magnons in yttrium iron garnet films, *J. Phys. D* **50**, 143002 (2017).
- [26] Y. M. Bunkov *et al.*, Discovery of the classical Bose-Einstein condensation of magnons in solid antiferromagnets, *JETP Lett.* **94**, 68 (2011).
- [27] Y. M. Bunkov and G. E. Volovik, Magnon Bose-Einstein condensation and spin superfluidity, *J. Phys.: Condens. Matter* **22**, 164210 (2010).
- [28] S. Autti, V. V. Dmitriev, J. T. Mäkinen, J. Rysti, A. A. Soldatov, G. E. Volovik, A. N. Yudin, and V. B. Eltsov, Bose-Einstein Condensation of Magnons and Spin Superfluidity in the Polar Phase of  $^3\text{He}$ , *Phys. Rev. Lett.* **121**, 025303 (2018).
- [29] Y. M. Bunkov and G. E. Volovik, Magnon Condensation into a  $Q$  ball in  $^3\text{He}-B$ , *Phys. Rev. Lett.* **98**, 265302 (2007).
- [30] A. A. Serga *et al.*, Bose-Einstein condensation in an ultra-hot gas of pumped magnons, *Nat. Commun.* **5**, 3452 (2014).
- [31] A. J. E. Kreil, D. A. Bozhko, H. Yu. Musiienko-Shmarova, V. I. Vasyuchka, V. S. L'vov, A. Pomyalov, B. Hillebrands, and A. A. Serga, From Kinetic Instability to Bose-Einstein Condensation and Magnon Supercurrents, *Phys. Rev. Lett.* **121**, 077203 (2018).
- [32] G. A. Melkov, V. L. Safonov, A. Yu. Taranenko, and S. V. Sholomkin, Kinetic instability and Bose condensation of nonequilibrium magnons, *J. Magn. Magn. Mater.* **132**, 180 (1994).
- [33] V. Zapf, M. Jaime, and C. D. Batista, Bose-Einstein condensation in quantum magnets, *Rev. Mod. Phys.* **86**, 563 (2014).
- [34] Y. M. Bunkov and V. L. Safonov, Magnon condensation and spin superfluidity, *J. Magn. Magn. Mater.* **452**, 30 (2018).
- [35] P. Pirro, V. I. Vasyuchka, A. A. Serga, and B. Hillebrands, Advances in coherent magnonics, *Nat. Rev. Mater.* **6**, 1114 (2021).
- [36] T. Byrnes, N. Y. Kim, and Y. Yamamoto, Exciton-polariton condensates, *Nat. Phys.* **10**, 803 (2014).
- [37] J. D. Plumhof, T. Stöferle, L. Mai, U. Scherf, and R. F. Mahrt, Room-temperature Bose-Einstein condensation of cavity exciton-polaritons in a polymer, *Nat. Mater.* **13**, 247 (2014).
- [38] B. T. Walker *et al.*, Driven-dissipative non-equilibrium Bose-Einstein condensation of less than ten photons, *Nat. Phys.* **14**, 1173 (2018).
- [39] T. K. Hakala *et al.*, Bose-Einstein condensation in a plasmonic lattice, *Nat. Phys.* **14**, 739 (2018).
- [40] A. I. Väkeväinen *et al.*, Sub-picosecond thermalization dynamics in condensation of strongly coupled lattice plasmons, *Nat. Commun.* **11**, 3139 (2020).
- [41] H. Deng, H. Haug, and Y. Yamamoto, Exciton-polariton Bose-Einstein condensation, *Rev. Mod. Phys.* **82**, 1489 (2010).
- [42] L. M. Sieberer, S. D. Huber, E. Altman, and S. Diehl, Dynamical Critical Phenomena in Driven-Dissipative Systems, *Phys. Rev. Lett.* **110**, 195301 (2013).
- [43] L. M. Sieberer, S. D. Huber, E. Altman, and S. Diehl, Nonequilibrium functional renormalization for driven-dissipative Bose-Einstein condensation, *Phys. Rev. B* **89**, 134310 (2014).
- [44] A. Rückriegel and P. Kopietz, Rayleigh-Jeans Condensation of Pumped Magnons in Thin-Film Ferromagnets, *Phys. Rev. Lett.* **115**, 157203 (2015).
- [45] M. Mohseni *et al.*, Bose-Einstein condensation of nonequilibrium magnons in confined systems, *New J. Phys.* **22**, 083080 (2020).
- [46] V. E. Zakharov, V. S. L'vov, and S. S. Starobinets, Spin-wave turbulence beyond the parametric excitation threshold, *Sov. Phys. Usp.* **17**, 896 (1975).
- [47] S. M. Rezende, Theory of coherence in Bose-Einstein condensation phenomena in a microwave-driven interacting magnon gas, *Phys. Rev. B* **79**, 174411 (2009).
- [48] L. J. Cornelissen, K. J. H. Peters, G. E. W. Bauer, R. A. Duine, and B. J. van Wees, Magnon spin transport driven by the magnon chemical potential in a magnetic insulator, *Phys. Rev. B* **94**, 014412 (2016).
- [49] M. Schneider *et al.*, Bose-Einstein condensation of quasiparticles by rapid cooling, *Nat. Nanotechnol.* **15**, 457 (2020).
- [50] L. D'Alessio and M. Rigol, Long-Time Behavior of Isolated Periodically Driven Interacting Lattice Systems, *Phys. Rev. X* **4**, 041048 (2014).
- [51] J. Tindall, B. Buča, J. R. Coulthard, and D. Jaksch, Heating-Induced Long-Range  $\eta$  Pairing in the Hubbard Model, *Phys. Rev. Lett.* **123**, 030603 (2019).
- [52] D. A. Abanin, W. De Roeck, W. W. Ho, and F. Huveneers, Effective Hamiltonians, prethermalization, and slow energy absorption in periodically driven many-body systems, *Phys. Rev. B* **95**, 014112 (2017).
- [53] D. Abanin, W. De Roeck, W. W. Ho, and F. Huveneers, A Rigorous Theory of Many-Body Prethermalization for Periodically Driven and Closed Quantum Systems, *Commun. Math. Phys.* **354**, 809 (2017).
- [54] W. W. Ho, I. Protopopov, and D. A. Abanin, Bounds on Energy Absorption and Prethermalization in Quantum Systems with Long-Range Interactions, *Phys. Rev. Lett.* **120**, 200601 (2018).
- [55] T. Kuwahara, T. Mori, and K. Saito, Floquet-Magnus theory and generic transient dynamics in periodically driven many-body quantum systems, *Ann. Phys. (NY)* **367**, 96 (2016).

- [56] T. Mori, T. Kuwahara, and K. Saito, Rigorous Bound on Energy Absorption and Generic Relaxation in Periodically Driven Quantum Systems, *Phys. Rev. Lett.* **116**, 120401 (2016).
- [57] T. Mori, T. N. Ikeda, E. Kaminishi, and M. Ueda, Thermalization and prethermalization in isolated quantum systems: A theoretical overview, *J. Phys. B* **51**, 112001 (2018).
- [58] T. Holstein and H. Primakoff, Field Dependence of the Intrinsic Domain Magnetization of a Ferromagnet, *Phys. Rev.* **58**, 1098 (1940).
- [59] N. Walldorf, D. M. Kennes, J. Paaske, and A. J. Millis, The antiferromagnetic phase of the Floquet-driven Hubbard model, *Phys. Rev. B* **100**, 121110(R) (2019).
- [60] Here, all integrals are understood as being properly normalized over the magnetic Brillouin zone.
- [61] For a corresponding analysis in the limit of weak driving,  $g < 1$ , see Appendix C.
- [62] We have checked that this slow timescale that emerges in the critical system is observed not only for the dynamics of the magnon number but also for the total energy as well as the magnon occupation at any given energy.
- [63] D. G. Mazzone *et al.*, Laser-induced transient magnons in  $\text{Sr}_3\text{Ir}_2\text{O}_7$  throughout the Brillouin zone, *Proc. Natl. Acad. Sci. USA* **118** (2021).
- [64] G. Falkovich and K. R. Sreenivasan, Lessons from hydrodynamic turbulence, *Phys. Today* **59**(4), 43 (2006).
- [65] J. Berges, Nonequilibrium quantum fields: From cold atoms to cosmology, [arXiv:1503.02907](https://arxiv.org/abs/1503.02907).
- [66] S. Erne, R. Bücke, T. Gasenzer, J. Berges, and J. Schmiedmayer, Universal dynamics in an isolated one-dimensional Bose gas far from equilibrium, *Nature (London)* **563**, 225 (2018).
- [67] S. Bhattacharyya, J. F. Rodriguez-Nieva, and E. Demler, Universal Prethermal Dynamics in Heisenberg Ferromagnets, *Phys. Rev. Lett.* **125**, 230601 (2020).